fluids

MDPI

Article

Reducing Flow Resistance via Introduction and Enlargement of Microcracks in Convection Enhanced Delivery (CED) in Porous Tumors †

Md Jawed Naseem, Ronghui Ma and Liang Zhu *

Department of Mechanical Engineering, University of Maryland Baltimore County, Baltimore, MD 21250, USA; mnaseem1@umbc.edu (M.J.N.); roma@umbc.edu (R.M.)

* Correspondence: zliang@umbc.edu; Tel.: +1-410-455-3332

† A portion of the this research was published in an extended abstract in the Summer Biomechanics, Bioengineering and Biotransport conference in June 2024 in Lake Geneva, WI, USA.

Abstract: A theoretical simulation is performed to evaluate how microcracks affect the flow resistance in tumors during the convection-enhanced delivery (CED) of nanofluids. Both Darcy's law and the theory of poroelasticity are used to understand fluid transport with or without microcrack introduction and/or enlargement. The results demonstrate significantly altered pressure and velocity fields in a spherical tumor with a radius of 10 mm due to the presence of a microcrack with a radius of 0.05 mm and length of 3 mm. The non-uniform fluid pressure field enlarges the original cylindrical microcrack to a frustum, with the crack volume more than doubled. Due to the larger permeability and porosity in the microcrack, flow in the tumor is much easier. One finds that the flow resistance with the enlarged microcrack is reduced by 14% from the control without a microcrack. Parametric studies are conducted to show that larger crack radii, longer crack lengths and higher infusing pressures result in further resistance reductions. The largest resistance reduction occurs when the infusing pressure is 4×10^5 Pa and the microcrack is 9 mm long, up to 18% from the control. We conclude that introducing a microcrack is an effective way to facilitate nanofluid delivery in porous tumors using CED.

Keywords: drug delivery; porous tumors; convection-enhanced delivery (CED); microcrack; tumor tissue deformation; flow resistance; nanofluid

Citation: Naseem, M.J.; Ma, R.; Zhu, L. Reducing Flow Resistance via Introduction and Enlargement of Microcracks in Convection Enhanced Delivery (CED) in Porous Tumors. *Fluids* **2024**, *9*, 215. https://doi.org/10.3390/fluids9090215

Received: 9 August 2024
Revised: 6 September 2024
Accepted: 9 September 2024
Published: 13 September 2024

1. Introduction

Medical advancements have enhanced the 5-year survival rates among cancer patients recently; however, clinicians still encounter considerable obstacles in planning effective treatment approaches to transport anti-cancer medications to tumors while alleviating the toxicity associated with drug accumulation in healthy organs and tissue. Drug delivery to solid tumors usually involves intravenous injection. The drug payload is often low using this approach, with less than 5% of the systemically injected drug eventually reaching the targeted tumor, while the majority of the drug is either cleared by the liver, spleen, or kidneys or deposited in other healthy tissue regions [1]. In addition, this approach is not suitable for poorly perfused and large-sized tumors. Some tumors at the late growth stages often form a necrotic/hypoxic core at the center, relying on the minimal supply of oxygen to survive [2]. Further, the systemic delivery of drugs may not be effective in brain tumor treatment because of the blood–brain barrier (BBB) [3]. To overcome the challenges faced by systemic delivery due to the presence of the BBB or limited blood perfusion, intratumoral infusion via convection-enhanced delivery (CED) has been proposed by means of single-port or multiple-port needles. This method has been widely used to deliver a variety of large therapeutic agents in tumors by the continuous injection of a drug-carrying nanofluid under a pressure difference [4–7]. With CED, therapeutic agents

may achieve tissue penetration of a few centimeters, unlike systemic delivery, which can only achieve a depth of micrometers from the capillary pores [8–10].

Several limitations have been noted in the past few decades when using CED. Among these are backflow along the needle, air bubbles, edema, and drug concentration heterogeneity. Backflow, also known as reflux, occurs when a catheter disrupts tissue sufficiently to create a void along its insertion tract, leading to a fluid-filled gap between the needle and tissue. This allows infusates to flow back along the catheter, rather than into the targeted tumor tissue [10]. Clinical studies have reported severe reflex pain experienced by patients with liver tumors when ethanol was injected directly into the tumor and leaked to the healthy tissue [11].

Previous studies have shed light on various factors that influence backflow to improve the drug delivery efficacy. Orozco et al. [12,13] used a three-dimensional finite element model to evaluate the infusion parameters of backflow during CED in the brain. Their findings underscore the relevance of the distance between the infusion cannula and the ventricles in limiting backflow, with long distances resulting in comparable backflow lengths independently of the ventricular pressure [12]. They also found that greater insertion speeds provided a larger pre-stress field, reducing the backflow duration over a range of flow rates. The study's experimental validation in agarose gel phantoms confirmed the predictions, with a significant decrease in the backflow length as the insertion speeds were increased [13]. Ayers and Smith [14] used a unique biphasic fluid–structure interaction (FSI) model to mimic infusion processes in agarose gel. Their model correctly recreated the experimental backflow lengths and maximum fluid pressures [14]. A major discovery indicates that small catheters, which require greater infusion pressures to achieve the appropriate medication distribution, often lead to intensive backflow. Theoretical studies by our group [15] showed that higher infusion rates, larger needle diameters, and lower elastic moduli yield longer backflow lengths and cause more irregular spreading shapes in the nanofluid. Together, these investigations have added greatly to the understanding of backflow in CED and provided vital insights into techniques for the optimization of medication delivery to tumors, thus leading to enhanced treatment outcomes [12–15].

Soft and thin catheters, as well as new "step-design" catheters, have been shown to reduce backflow [16–18]. Several improvements in cannula design have implemented flexible cannulas, resulting in increased infusion rates, reduced backflow, and increased fluid volumes through the cannula-induced track. Some experimental results have demonstrated that CED using catheters with larger diameters is more likely to lead to reflux [19–21]. This observation resulted in a step-down catheter design called a reflex-preventing catheter [22]. Multiport catheters were originally designed for hydrocephalus. Later, they were adapted for CED due to their potential for better volume distribution [6]. However, achieving predictable flows from all ports proved challenging, often resulting in infusates flowing only through the most proximal port. The proposed solutions included using porous materials to spread the infusion area, developing catheters with separate lumens, or using catheters with controllable portholes. A breakthrough came with Twin Star Medical's development of a hollow-fiber catheter [23], which contains millions of tiny openings (0.45 µm) along its wall surface [23]. This design has successfully increased infusate transfer up to three-fold, improved the uniformity of distribution, and reduced backflow, therefore making it a promising advancement in CED technology [23]. The balloon-tipped catheter approach uses a balloon near the catheter tip to fill the resection cavity, pushing the infusate into the cavity and limiting reflux [22]. Studies in canine models have shown the extensive delivery of infusates [22].

The company Rex Medical (Conshohocken, PA) recently developed an infusion catheter (Quadra Fuse ST) consisting of three retractable injection tines. The tines are hidden inside a hosting catheter initially. At the end of the hollow catheter, 10 mm hollow tines with sharp tips are attached for the piercing of tissue. After the catheter is inserted into the targeted tissue, the three tines can be ejected in three directions and therapeutic fluid then flows from their tips. This device also allows repeated infusion. After the first

round of infusion, the tines are retracted back to the hosting catheter; one then rotates the hosting catheter by 60°, resulting in three new ejection directions of the tines. The original design of this device aims at using the tines for infusion improvement, and the retracting ability of the tines allows more infusing sites to enlarge the infused tissue volume. Clinical studies have demonstrated the efficiency of this device in delivering ethanol to liver tumors [11,24]. They found that, with the traditional single-needle infusion of ethanol to liver tumors, patients often expressed severe pain, possibly due to the leakage of the ethanol through the backflow channel to the surrounding healthy tissue. After they employed the retractable-tine catheter, less pain was experienced by the patients, implying less leakage of ethanol to healthy tissue with sensory nerves [11,24].

Backflow, in principle, is largely due to tissue deformation. There have been several studies that have evaluated the enlargement of the generated gap between the infusion catheter and the tissue [14,15]. In principle, any methods to make the flow easier in the tumor would minimize backflow. None of the previous studies have evaluated a CED system with a retractable tine, especially the effects of the retractable tines on the generation of microcracks in tumors and the resulting change in flow resistance in tumors during direct fluid infusion. In this study, we aim to develop theoretical models to evaluate how the introduction of a microcrack in the tissue reduces the overall flow resistance in a porous tumor, as well as further decreasing the flow resistance as this microcrack enlarges in a direct infusion process using CED. Both Darcy's law and the theory of poroelasticity are used in the simulation to understand the fluid transport in porous tumors with or without microcrack introduction and/or enlargement. We expect that the study will provide quantitative measures to evaluate whether this approach is effective to enhance nanofluid transport in dense porous tumors.

2. Materials and Methods

2.1. Model Setup

In this study, a tumor is modeled as a fully saturated, spherical, porous medium with a radius of 10 mm (r_o = 10 mm). The interstitial fluid inside the tumor is assumed as a Newtonian fluid and intrinsically incompressible. The tumor is considered spatially homogeneous with uniform biological and physical properties. The infusion needle track is omitted in this study because our aim is to evaluate the role played by microcrack induction and enlargement. As shown in Figure 1, the convection-enhanced fluid infusion at the needle tip is simplified as a fluid flow passing a spherical surface with a radius of r_i = 0.64 mm, which is equivalent to the opening of a 18 G Hamilton needle in direct infusion. The fluid infusion site is modeled as a surface with a prescribed pressure (P_0) as a driving force for the fluid flow.

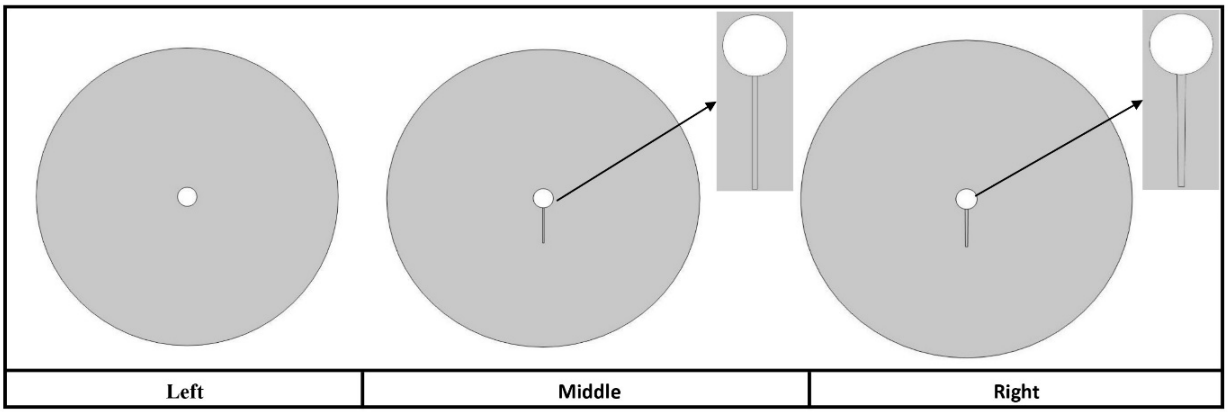

Figure 1. Three models generated in this study for simulation. (**Left**): the first model without a crack; (**middle**): the second model with a cylindrical microcrack; and (**right**): the third model with an enlarged microcrack.

We construct three tumor models for the comparison of the flow resistance with or without a microcrack, as well as with or without microcrack enlargement. The first model, or the control, represents a porous tumor without a microcrack. A cylindrical microcrack is included in the second model, shown in the middle panel of Figure 1. The microcrack is modeled as a cylindrical column that is initiated in the infusion surface and extended to the tumor periphery. Both the microcrack and the remaining tumor region are modeled as porous media with individual porosities and permeabilities. The interstitial fluid pressure field using Darcy's law is the input needed for the poroelastic simulation to predict the tissue deformation and microcrack enlargement during the infusion process. It would be ideal to have the Darcy's pressure field coupled with the tissue deformation in the second model. Unfortunately, the computational software that we use only allows one-way coupling, i.e., it does not allow the update of the pressure field after tissue deformation. Thus, we construct the third model, in which an enlarged microcrack is included, as shown in the right panel of Figure 1. The geometry of the enlargement of the microcrack is exported from the poroelastic simulation of tissue deformation from the second model. The shape and the geometry of the microcrack after enlargement are then regenerated in the software and introduced to the porous tumor. Both the microcrack and the remaining tumor region are again modeled as uniform porous media with respective porosities and permeabilities. In the third model, only Darcy's law is needed to update the pressure and velocity fields. Although, in theory, the updated pressure field would further affect the tissue deformation, due to the limitations of our software, we are not able to truly couple the fluid pressure and tissue deformation in the poroelastic simulation. Therefore, the current study is viewed as reflecting the lower limit of tissue deformation and microcrack enlargement.

2.2. Governing Equations

Directly after the initiation of fluid infusion, both the fluid field and tissue deformation are assumed to occur instantaneously, and the focus of this research is on the resultant deformation rather than the deforming process. Thus, the system including fluid flow and tissue deformation is considered to be in a steady state.

In this study, the tumor tissue is treated as porous media, reflecting a structure comprising a solid matrix interspersed with interconnected pores or void spaces. The pores inside the tumor are saturated before the infusion. The theory of Darcy's law [25] is used to describe how fluid flows in tissue, which is given by

$$\nabla \cdot \left(\phi \vec{V}_f \right) = 0 \tag{1}$$

$$\nabla P_f = -\frac{\mu \phi}{K} \vec{V}_f \tag{2}$$

where $\vec{V}_f$ is the interstitial fluid velocity vector, P_f is the interstitial fluid pressure, μ is the fluid dynamic viscosity, ϕ is the tumor porosity, and K is the permeability of the porous tumor.

As shown in Figure 1, with the microcrack, there are two porous medium regions. The first region is the porous tumor tissue with a radius of 10 mm, having permeability $K_1 = 5 \times 10^{-16}$ m^2 and porosity $\phi_1 = 0.2$ [15]. The microcrack is modeled as the second porous medium region with much greater permeability K_2 and porosity ϕ_2. It is well known that tissue consists of three major regions: the interstitial fluid space, the extracellular matrix, and the cells. Porosity is defined as the ratio of the volume of the interstitial fluid space to the total tissue volume. When a tine pierces the tissue, one could assume that all cells on the piercing pathway would be damaged to release all fluid inside. This would enlarge the interstitial fluid space tremendously. Previous research [26] has stated that the extracellular fluid space occupies approximately 20% of the region of a tumor. After being pierced by the tine, the microcrack only has the extracellular matrix and the interstitial

fluid space remaining. The porosity of the microcrack region can then be calculated as 100% − 20% = 80%, or $\phi_2 = 0.8$.

It is well known that a tumor's permeability is closely related to its porosity. We use the relationship between the porosity of deformed tissue and tissue dilatation e from previous studies [27,28]:

$$\phi_2 = \frac{\phi_1 + e}{1 + e} \tag{3}$$

Substituting the values of the two porosities into the above equation yields a dilation value e equal to 3. To quantify the permeability K as a function of dilatation e, we use the relationship given by Lai and Mow [29] as

$$K_2 = K_1 \exp(M * e) \tag{4}$$

where K_1 is the permeability in the absence of deformation, and M is a material constant that governs the variation in the permeability with deformation. For simplicity [15,28–30], we use the value $M = 2$. Substituting the value of $e = 3$ into the above equation leads to the following calculation:

$$K_2 = 403.26\ K_1 \tag{5}$$

Equations (1) and (2) can be combined into a governing equation for the pressure field in the interstitial fluid space, P_f, as

$$\nabla^2 P_f = 0 \tag{6}$$

The interstitial fluid pressure can be solved first with appropriate boundary conditions. The boundary conditions, required to solve the pressure field, consist of a prescribed pressure P_0 at the inner spherical surface representing the infusion surface. At the tumor's outer surface ($r = r_o$), its pressure is zero. This is an assumption, since tumors may be surrounded by tissue at different pressure levels, and liquid transport is dominated by the pressure gradient rather than the absolute pressure values. The boundary conditions of the pressure field are written as

$$\begin{aligned} r &= r_o, \quad P_f = 0 \\ r &= r_i, \quad P_f = P_0 \end{aligned} \tag{7}$$

The deformation of a purely elastic material is proportional to the imposed stress developed either externally due to the behavior of the surrounding normal tissue or internally by its own growth [15,31,32]. In a porous tumor, the fluid pressure in the interstitial fluid space is not uniform during direct fluid infusion. The non-uniformity of the fluid pressure would place extra displacements and strains on the tissue. In the theory of poroelasticity, the fluid pressure is included in the governing equation for tissue deformation as

$$G\nabla^2 \vec{u} + (\lambda + G)\nabla\left(\nabla \cdot \vec{u}\right) = \nabla\left(\phi P_f\right) \tag{8}$$

where $\vec{u}$ is the tissue displacement vector; G and λ are Lame constants that can be determined by Young's modulus E and Poisson's ratio v using the following expressions:

$$\lambda = \frac{Ev}{(1+v)(1-2v)};\ G = \frac{E}{2(1+v)} \tag{9}$$

Boundary conditions are needed to solve the tissue displacement field. The outer boundary of the tumor is fixed in space, indicating zero displacement. Although the infusion cavity may also be pushed in the radial direction, in this study, we assume that the inside spherical surface is subjected to a roller constraint, i.e., the displacement is zero in the direction perpendicular to the boundary but the boundary is free to move in the tangential direction. The boundary conditions are written as

$$r = r_o \quad \vec{u} = 0 \tag{10}$$

$$r = r_i \quad \vec{u} \cdot \vec{n} = 0$$

2.3. Solving Procedures

In this study, the first model in Figure 1 utilizes Darcy's law to simulate the pressure and velocity fields during a direct fluid infusion process, and it is used to estimate the flow resistance of the control without any microcracks. The second model aims to demonstrate the influence of the non-uniform interstitial fluid pressure field due to the introduction of a microcrack on tissue deformation, especially in the microcrack region. The displacement vector along the microcrack is then exported from the second model and analyzed in Excel (Microsoft EXCEL 2016) to acquire the shape change of the microcrack from the original cylinder to an approximate wedge shape. Excel also allows the approximation of the enlarged microcrack by a simplified frustum shape to be imported to the third model. The third model with the enlarged microcrack is used to assess how the fluid field is affected by the enlargement in the microcrack during the fluid infusion.

In each model, the volumetric flow rate is calculated by integrating the normal fluid velocity over the outer surface of the tumor. The flow resistance is defined as the pressure difference between the infusion needle and the tumor's outer surface divided by the calculated volumetric flow rate (Q_{outer}) and is given by

$$R_{flow} = \frac{P_o - 0}{Q_{outer}} \tag{11}$$

2.4. Numerical Simulation Methods

The governing equations are solved using the multi-physics platform of the COMSOL software package (version 6.1, COMSOL Inc., Stockholm, Sweden) under the Sub-surface module, which can handle poroelastic modeling to determine the deformation of tissue when subjected to a fluid field in a porous medium. The simulation domain is two-dimensional axis-symmetric. The meshes of the geometry are generated by the software. A direct linear solver, the Multifrontal Massively Parallel Sparse Direct Solver (MUMPS), with a default pre-ordering algorithm is used to solve the poroelastic model, while the Parallel Sparse Direct Solver (PARDISO) is used to solve the pressure and velocity fields.

The sensitivity to the mesh size is evaluated to ensure the accuracy of the numerical simulation. Table 1 shows how varying mesh sizes affect the results of the volumetric flow rate on the tumor surface during infusion in the tumor with the introduction of a microcrack. It illustrates that a 100% increase in the number of mesh elements, from a finer mesh setting (1764 elements) to an extra fine mesh setting (3845 elements), results in a negligible alteration of less than 0.14% in the volumetric flow rate. A further increase in the total number of the elements to 12,879 using the setting of an extremely fine mesh only changes the result by less than 0.04%. Further, the numerical simulation results of the pressure field in the first model were compared to an analytic solution in a one-dimensional porous medium pressure field. It was found that the numerical simulation results of the pressure fields agreed very well with the prediction using the analytical solution, with deviations of less than 0.01%.

Table 1. Sensitivity of simulated results to mesh size.

Mesh Type	# of Triangular Elements	Q_{outer} m^3/s
Extremely fine	12,879	9.451×10^{-10}
Extra fine	3845	9.4475×10^{-10}
Finer	1764	9.4348×10^{-10}
Fine	1160	9.413×10^{-10}

3. Results

3.1. Parameters

The geometric parameters of the tumor, the infusion site, and the microcrack are listed in Table 2. The infusion needle is an 18 G needle with a radius of 0.64 mm, representing the radius of the infusion's spherical surface. The microcrack is formed due to a tine injection and retraction. The tine has a size of 25 G, being approximately 0.207 mm in radius. Considering that, after the tine's retraction, the tissue would bounce back, resulting in a much smaller radius than that of the tine, in this study, we select the radius of the microcrack as 0.025 mm or 0.05 mm. Several possible lengths of the tine/microcrack are selected, varying from 3 mm to 9 mm.

Table 2. Geometrical parameters used in the simulation.

Geometrical Parameter	Value
Infusion surface radius r_i	**0.64** mm
Tumor outer radius r_o	**10** mm
Microcrack radius without enlargement	0.025 or **0.05** mm
Microcrack length	**3 mm**, 4.5 mm, 6 mm, 7.5 mm, or 9 mm

The fluid transport properties in the porous tumor and the solid mechanical properties of the tissue are summarized in Table 3. All fluid transport properties are obtained from the literature or derived as described in the previous section. The properties of the solid tumor, including the density, Young's modulus, and Poisson's ratio, are found from previous research [4,15,28,33–35]. The solid mechanical properties of the microcrack are unknown. In theory, this microcrack domain should be modeled as a fluid by the traditional Navier–Stokes equations. Unfortunately, our simulation module in COMSOL does not allow the selection of this domain as a purely liquid domain. Considering that the microcrack domain is very close to a liquid domain, we select a small Young's modulus for this domain without causing simulation singularities. With this approximation, the simulation result from the current study can be considered as the lower limit of microcrack enlargement, as the enlargement of the microcrack would have been larger if the domain was treated as a purely liquid domain.

Table 3. Fluid and mechanical properties used in the simulation [4,15,28,33–35].

Fluid Property		Mechanical Property	
Density of tumor ρ	1000 kg/m^3	Tumor Young's module E_1	0.3 MPa [28,33]
Tumor porosity ϕ_1	0.2 [34,35]	Crack Young's module E_2	0.003 MPa
Crack porosity ϕ_2	0.78, **0.8**, 0.81	Tissue Poisson's ratio ν_1	0.4 [4,28]
Tumor permeability K_1	5×10^{-16} m^2 [28,34]	Crack Poisson's ratio ν_2	0.4 [4,28]
Crack permeability K_2	1×10^{-13}, $\mathbf{2.0173 \times 10^{-13}}$, 3×10^{-13} m^2		
Infusion pressure P_0	10^5, $\mathbf{2 \times 10^5}$, 4×10^5 Pa [15]		
Dynamic viscosity μ	10^{-3} Pa s [15]		

3.2. Baseline Case Simulation Results

3.2.1. Pressure and Velocity Fields without Introduction of Microcrack [36]

In both Tables 2 and 3, the bold properties or parameters represent those used in the baseline case before the parametric study. The control used in our simulation considers a tumor with a radius of 10 mm, with a fluid infused from a spherical surface having a radius of 0.64 mm. The outside boundary condition for the fluid is maintained at zero pressure, while the pressure at the infusion surface is selected as 2×10^5 Pa, as shown in Table 3.

Without the introduction of a microcrack, the pressure field is one-dimensional, depending only on the radial direction in the spherical coordinate system. Figure 2 gives the contours of the interstitial fluid pressure in the porous tumor, illustrating the satisfaction of the boundary conditions of the pressure field. A rapid decrease in pressure to 50% of its initial value can be seen when the distance from the infusion surface r = 1.286 mm, while it decreases to 10% of its initial value at r = 4.875 mm, less than halfway towards the tumor outer surface. This indicates that major fluid resistance occurs in the tumor's central region, rather than the tumor's periphery. Therefore, most of the tumor region towards the periphery appears blue. Figure 2 shows the velocity vector distribution in the tumor with an enlarged velocity field near the infusion surface. It is a clear directional flow away from the infusion surface, indicating the radial dispersion of the fluid through the tumor tissue. Based on the simulation parameters, the maximal velocity magnitude occurring at the infusion surface is 1.66×10^{-4} m/s. The magnitude of the velocity vector decreases in the radial direction and its magnitude at the tumor outer surface is 6.84×10^{-7} m/s, confirming the mass conservation in the simulation. As expected, both the pressure and velocity fields in the first model show their dependence on the radial coordinate r.

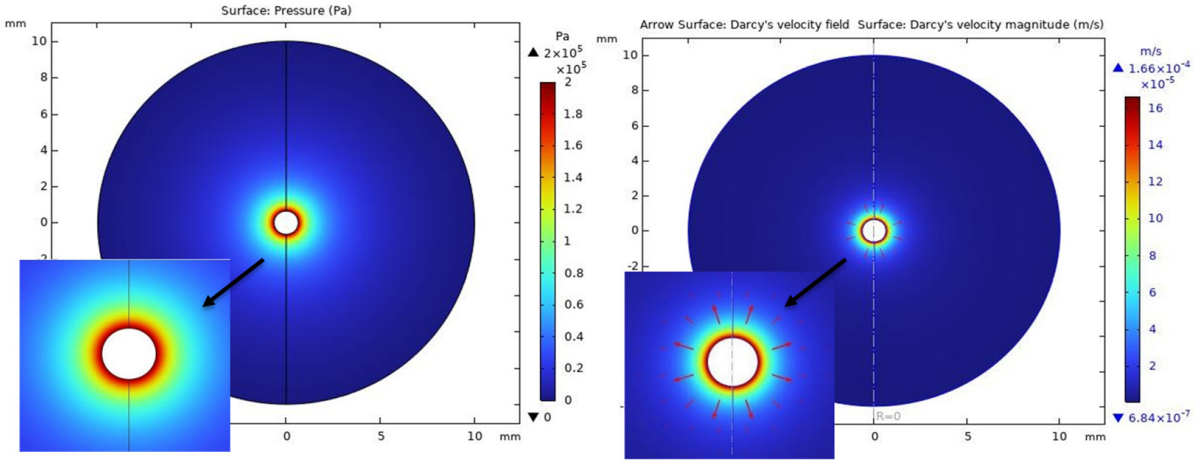

Figure 2. Simulated pressure field (**left**) and velocity field (**right**) in the tumor without a microcrack. The inset images are the enlarged pressure and velocity fields near the infusion surface.

3.2.2. Microcrack Introduction and Tissue Deformation by the Poroelastic Model

The effect of an introduced microcrack in the tumor is examined in the second model, in which the cylindrical microcrack has a radius of 0.05 mm and a length of 3 mm in the baseline case. Figure 3 gives the pressure field with the cylindrical microcrack. The inset image shows the enlarged pressure field near the infusion surface and along the microcrack. One observes that the maximal pressure again occurs at the tumor's central region, aligning with the prescribed boundary condition at the infusion surface. Since the permeability of the microcrack domain is much larger than that in the regular tumor region, the flow through the microcrack is much easier than that through the tumor. Figure 3 shows small pressure drops from the infusion surface to the tumor–microcrack interface, as if an extension of the isobaric contour from the original infusion surface. Therefore, the microcrack facilitates fluid transport to the tumor periphery surface by reduced resistance and a shortened distance. Figure 3 also provides the velocity field, where the velocity magnitude exhibits a peak of 0.0178 m/s along the microcrack near the infusion surface. It is also evident that the maximal magnitude of the velocity vector is two orders of magnitude higher than that in the first model without a microcrack. The minimal velocity at the tumor's outer surface increases by 3.9%, from 6.84×10^{-7} in the first model to 7.11×10^{-7} m/s. The large contrast in the velocity variation from the maximal to the minimal value results in the appearance of an almost bluish color in most of the tumor region, except near the infusion surface and along the microcrack path.

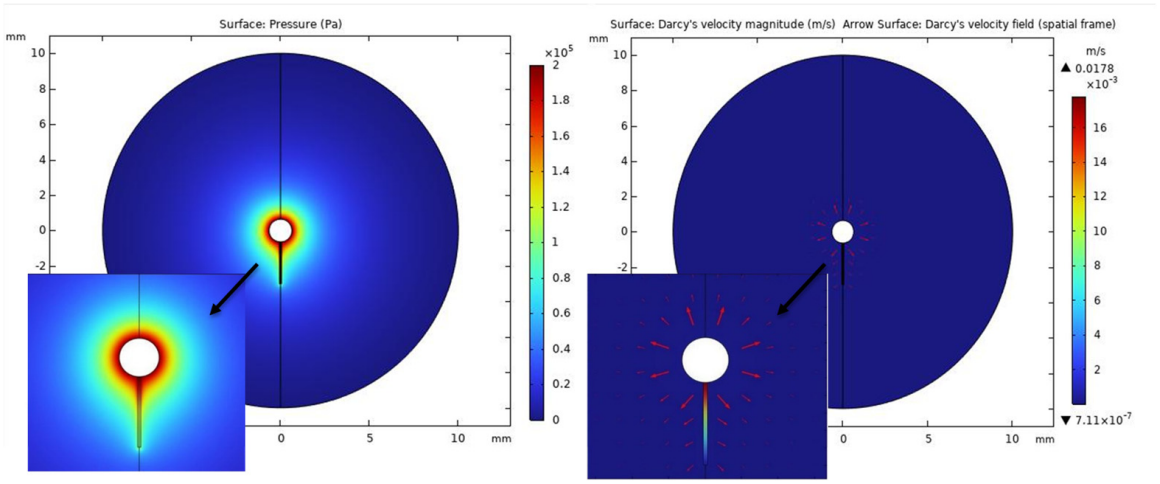

Figure 3. Simulated pressure field (**left**) and velocity field (**right**) in the tumor with a cylindrical microcrack. The inset images are the enlarged pressure and velocity fields near the infusion surface and along the microcrack.

The generated interstitial fluid pressure (P_f) from the Darcy model is given as an input to determine the deformation of the surrounding tumor tissue. Based on the poroelastic model described in the Section 2, the non-uniform interstitial fluid pressure is the major reason for the non-uniform displacement of the tissue during fluid infusion using CED. Two components of the displacement vector in the simulation domain are presented in Figure 4. In the direction perpendicular to the axis of the microcrack shown in the left panel, the displacement component perpendicular to the microcrack axis is positive everywhere, indicating that the tissue moves in this direction (the black arrows in the figure). One notices that the maximal displacement occurs near the central region, but not at the infusion surface, due to the prescribed roller boundary condition there. The maximal displacement in the lateral direction is less than 0.08 mm. On the other hand, in the direction along the microcrack axis, shown in the right panel, the negative values in the region around the vicinity of the microcrack indicate that the tissue moves downwards (blue color in the figure), while the red-colored region represents a positive value in the displacement component, suggesting that the tissue moves upward. One notes that the displacement surrounding the microcrack (the bluish region in the right panel) is around 0.0982 mm, which is larger than the region without a microcrack (the reddish region in the right panel).

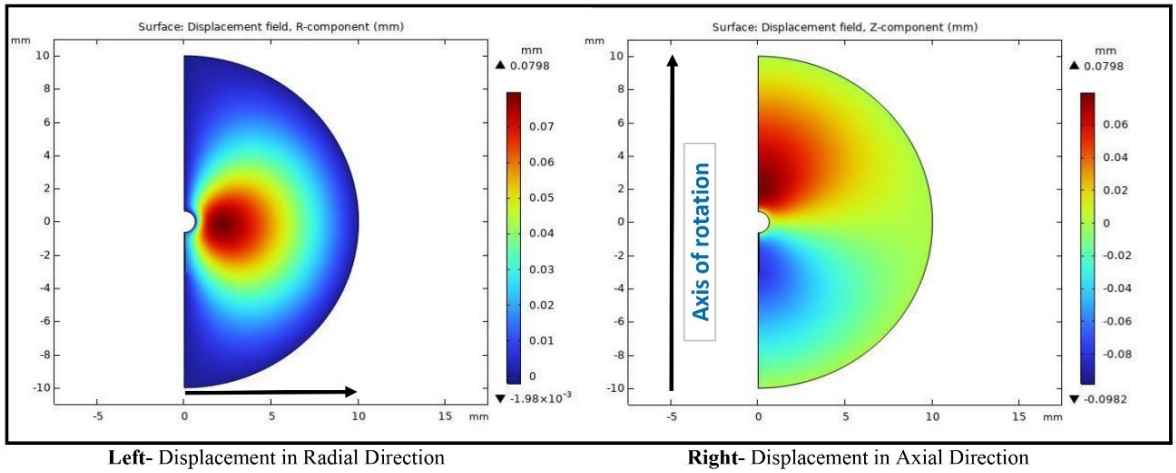

Figure 4. Components of the displacement vector in the lateral (**Left**) and axial (**Right**) directions of the microcrack in the tumor with a cylindrical microcrack.

The displacement vector determined in the poroelastic model can be exported to understand how the microcrack is enlarged due to the fluid infusion. In this study, we select the displacement vectors along the interface between the microcrack and tumor tissue for further analysis. As shown in Figure 5, the two components of the displacement vector are exported and plotted in Excel. The green dots in Figure 5 represent the original interface. After adding the two components of the displacement vector in the directions perpendicular to and along the microcrack axis, respectively, one can generate the new interface positions on the cross-sectional plane. The red dots in Figure 5 provide the new interface between the microcrack and tumor region. Overall, the magnitude of the displacement in the lateral direction of the interface varies from 0.025 mm near the infusion surface to 0.0073 mm at the tip of the microcrack, leading to a frustum-shaped crack. The deformation is significant since the original microcrack radius is 0.05 mm. The volume of the frustum is 2.26 times the value of the original cylindrical microcrack, due to the fluid infusion-induced tissue deformation. Using a curve fitting to the new interface, one can generate an approximated frustum microcrack. This simplified recreation of the enlarged microcrack serves as a basis for the third model to re-examine the pressure and velocity fields with the enlarged microcrack.

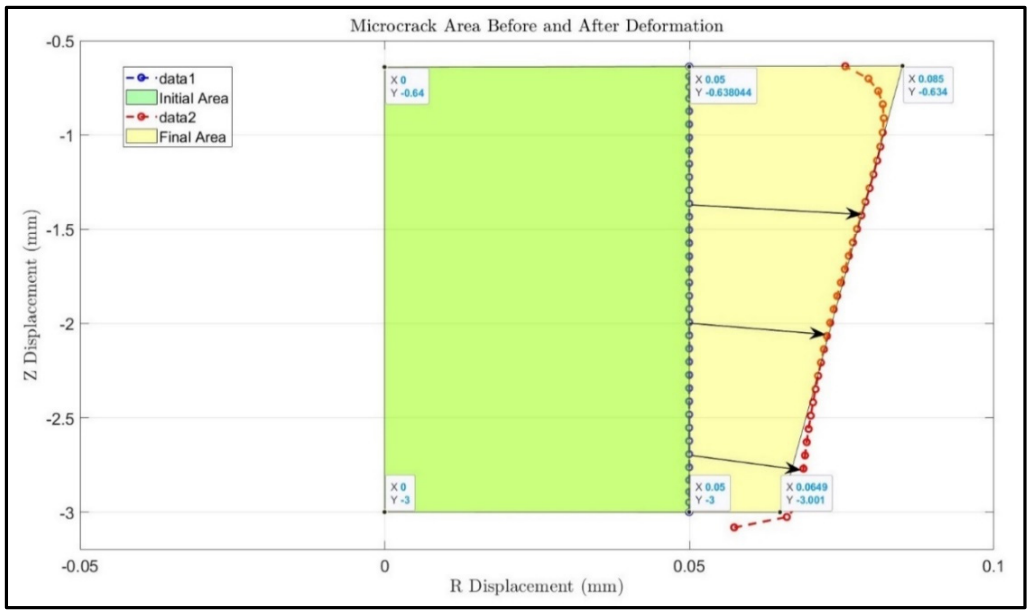

Figure 5. The original (green dots) interface and post-deformation (red dots) interface of the microcrack and tissue plotted in Excel. A frustum-shaped microcrack is generated using curve fitting.

3.2.3. The Enlarged Microcrack Constructed in the Third Model

The third model considers the fluid field in the tumor with a frustum-shaped microcrack, as reconstructed in the previous section. The rapid decrease in the interstitial fluid pressure with the enlarged microcrack is shown in Figure 6, appearing highly localized around the infusion surface and along the microcrack. Similar to Figure 3, there is a notable push towards the tumor's outer surface in the high-pressure region as compared to the control in the first model. This is due to the reduced resistance and shortened distance for the fluid to reach the tumor boundary with the formation of the frustum-shaped microcrack. When one examines the velocity field shown in Figure 6, the maximal velocity is 0.0106 m/s, which is of the same order of magnitude but smaller than that in the second model. This result may be explained by the larger cross-sectional area due to the lateral enlargement of the microcrack from the original radius of 0.05 mm to 0.085 mm. It is worth noting that the minimal velocity in the tumor with the enlarged microcrack is 7.29×10^{-7} m/s, the largest in the three models. Again, the large variation in the velocity field in the tumor causes the

color to appear bluish in most of the tumor, except near the infusion surface and along the microcrack path.

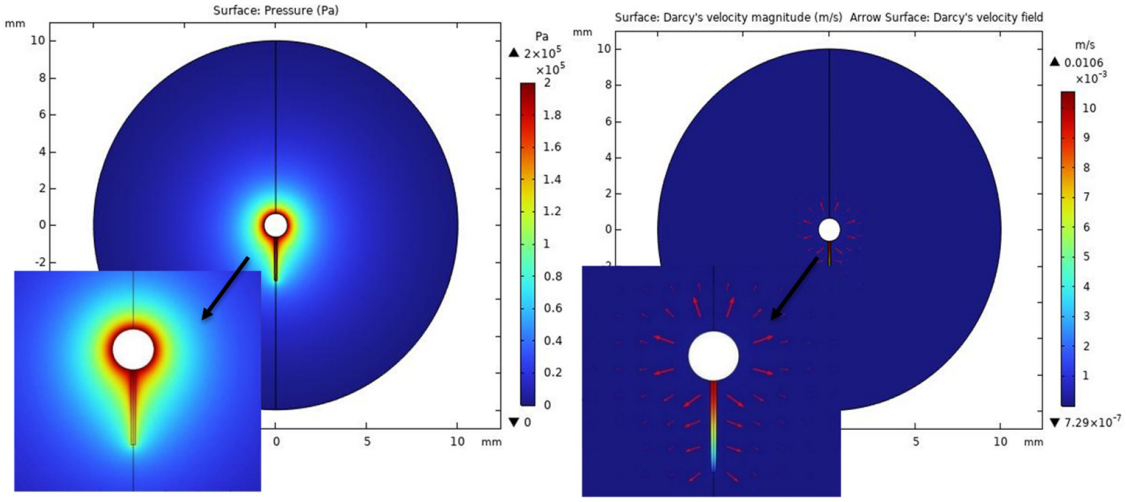

Figure 6. Simulated pressure field (**left**) and velocity field (**right**) in the tumor with an enlarged frustum microcrack. The inset images are the enlarged pressure and velocity fields near the infusion surface and along the microcrack after deformation.

3.2.4. Flow Rate and Flow Resistance

The volumetric flow rate can be calculated by integrating the velocity component normal to the outer surface of the tumor over the outer surface. Listed in Table 4 are the volumetric flow rates and flow resistance defined in Equation (11). The volumetric flow rate in the tumor without a microcrack is equal to 8.59×10^{-10} m^3/s under the pressure difference of 2×10^5 Pa. The introduction of a microcrack and the subsequent enlargement of the microcrack increase the volumetric flow rate by 10% and 11.6%, respectively. As seen in Table 4, a microcrack substantially decreases the flow resistance within the porous tumor. The introduction of a cylindrical microcrack to the spherical tumor decreases the flow resistance from 2.328×10^{14} Pa s/m^3 in the first model to 2.116×10^{14} Pa s/m^3 in the second model, by 9%. With the enlarged microcrack utilized in the third model, the flow resistance is further reduced from that in the second model. Overall, having an enlarged microcrack results in a decrease of 14% from the control without a microcrack.

Table 4. Volumetric flow rate on the tumor's outer surface and the flow resistance in the three models.

	The 1st Model	**The 2nd Model**	**The 3rd Model**
Q_{outer}, m^3/s	8.592×10^{-10}	9.451×10^{-10}	1.000×10^{-9}
R_{flow}, Pa s/m^3	2.328×10^{14}	2.116×10^{14}	1.999×10^{14}

3.3. Parametric Studies

This section quantifies how changes in one or more parameters or variables affect the simulation outcomes. The analysis will elucidate the direct implications of a microcrack for the fluid transport efficiency and flow resistance, while revealing pivotal insights to enhance fluid delivery to tumors.

3.3.1. Changing the Axial Length of the Microcrack

The geometry of the original cylindrical microcrack is determined by the retractable tine. In this study, we vary the length of the microcrack from 3 mm (the baseline case) to 9 mm to examine how the length of the microcrack affects the pressure and velocity fields, as well as the enlargement of the microcrack. The enlargement of the microcrack

due to tissue deformation is illustrated in Figure 7. It is unsurprising that we see almost the same lateral displacement near the infusion surface for different lengths of the microcrack, due to the same local fluid pressure of 2×10^5 Pa. As the fluid pressure decreases along the axial direction of the microcrack, the lateral displacement tapers. Note that the effect of microcrack enlargement significantly declines between 4.5 mm and 6 mm in the axial direction and almost disappears after 6 mm. This suggests the diminishing influence of the fluid pressure, which is unable to sustain further expansion along the microcrack.

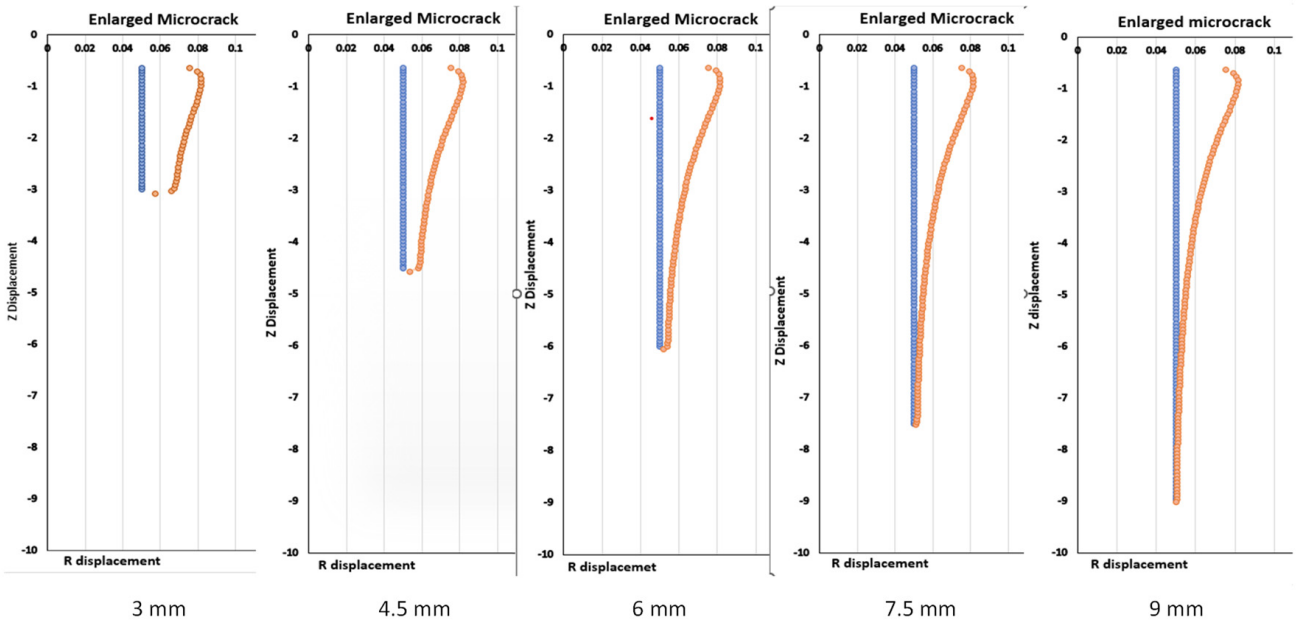

Figure 7. The original (blue dots) and post-deformation (orange dots) interfaces between the microcrack and tumor region, as affected by the length of the microcrack.

The obtained volumetric flow rate and flow resistance are shown in Tables 5 and 6. The impacts of the microcrack length are limited up to a certain threshold length, i.e., approximately 6 mm for the second model and the third model. After this threshold, further increases in the crack length would have a very minor effect on the volumetric flow rate and flow resistance. Compared to the baseline case of having a 3-mm-long microcrack, further increasing the crack length would enhance the volumetric flow rate by 1.5% in the second model with a cylindrical microcrack. In the third model with the enlarged microcrack, the percentage increase from its baseline case is slightly higher, up to 3.4%. The reductions in the flow resistance follow similar trends. With the longest microcrack length of 9 mm, the enlarged microcrack would decrease the flow resistance by more than 17% from the control without a microcrack in the tumor.

Table 5. Volumetric flow rate affected by changing the microcrack length.

Crack Length	Volumetric Flow Rate Q_{outer} (m^3/s)			Change from the Baseline Case	
	The 1st Model	The 2nd Model	The 3rd Model	The 2nd Model	The 3rd Model
3 mm	8.592×10^{-10}	9.451×10^{-10}	1.000×10^{-9}	NA	NA
4.5 mm	8.592×10^{-10}	9.568×10^{-10}	1.028×10^{-9}	1.3%	2.7%
6 mm	8.592×10^{-10}	9.596×10^{-10}	1.034×10^{-9}	1.5%	3.4%
7.5 mm	8.592×10^{-10}	9.604×10^{-10}	1.034×10^{-9}	1.6%	3.4%
9 mm	8.592×10^{-10}	9.607×10^{-10}	1.034×10^{-9}	1.7%	3.4%

Table 6. Calculated flow resistance for different microcrack lengths.

Crack Length	Flow Resistance R_{flow} (Pa s/m^3)			Change from the Baseline Case	
	The 1st Model	The 2nd Model	The 3rd Model	The 2nd Model	The 3rd Model
3 mm	2.328×10^{14}	2.116×10^{14}	1.999×10^{14}	NA	NA
4.5 mm	2.328×10^{14}	2.090×10^{14}	1.946×10^{14}	−1.2%	−2.7%
6 mm	2.328×10^{14}	2.084×10^{14}	1.934×10^{14}	−1.5%	−3.2%
7.5 mm	2.328×10^{14}	2.082×10^{14}	1.933×10^{14}	−1.6%	−3.3%
9 mm	2.328×10^{14}	2.081×10^{14}	1.934×10^{14}	−1.7%	−3.3%

3.3.2. Changing the Radius of the Initial Cylindrical Microcrack

We then examine the effect of the radius of the cylindrical microcrack on the fluid flow and the tissue deformation. The radius of 0.207 mm is the corresponding size of the tine, assuming no bounce. The extent to which the tissue bounces after the withdrawal of the tine is unclear. In this study, the unknown microcrack radius is assumed as either 0.025 mm or 0.05 mm when keeping the microcrack length the same as in the baseline case of 3 mm. Figure 8 shows the displacement of the microcrack–tumor interface as affected by the radius of the microcrack. It is evident that an overall higher pressure field within the microcrack would result in much larger tissue deformation and, thus, a larger shift in the crack–tumor interface towards the tumor periphery. Compared to the baseline case (radius = 0.05 mm) with a lateral displacement near the infusion surface of 0.03 mm, the lateral displacement decreases by 53% when the crack radius is 0.025 mm.

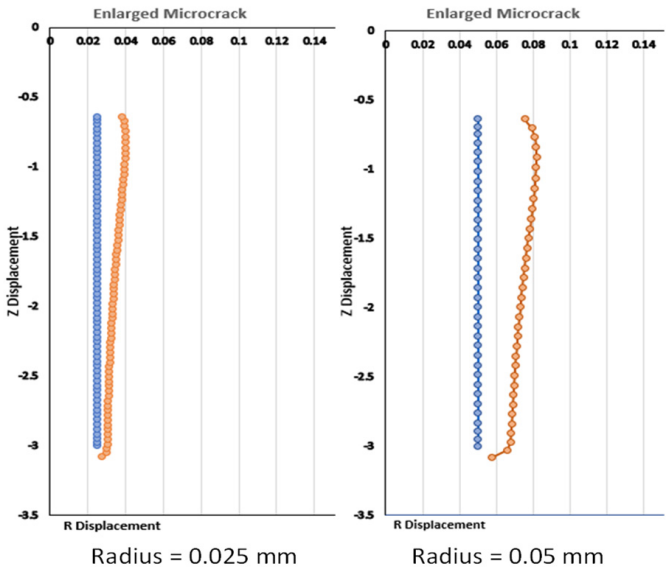

Figure 8. The original (blue dots) and post-deformation (orange dots) interfaces between the microcrack and tumor region, as affected by the radius of the original cylindrical microcrack.

Table 7 gives the results regarding how the radius of the cylindrical microcrack affects the flow resistance. In the baseline case with a microcrack radius of 0.05 mm, the maximal resistance reduction is 14%. In contrast, when the microcrack radius is 0.025 mm, the enlarged microcrack in the third model only results in a less than 6.5% reduction in the flow resistance when compared to the first model without a microcrack. The modest reduction indicates the diminishing influence of the microcrack with a smaller initial radius. Larger tissue rebouncing after the retraction of the tine would result in smaller overall tissue deformation and a smaller impact on the velocity and pressure fields.

Table 7. Flow resistance due to different microcrack radii.

Crack Radius	Flow Resistance (Pa s/m^3)			Reduction in Flow Resistance		
	1st Model	2nd Model	3rd Model	1st Model	2nd Model	3rd Model
0.025 mm	2.33×10^{14}	2.25×10^{14}	2.18×10^{14}	N/A	3.5%	6.5%
0.05 mm	2.33×10^{14}	2.12×10^{14}	2.00×10^{14}	N/A	9%	14%

3.3.3. Influence of the Transport Properties in the Microcrack

As shown in Table 3, two more cases of K_2 are included as it decreases or increases by 50% from the baseline value. The influence of the permeability of the microcrack on the pressure field is shown in Figure 9. When the permeability is doubled or tripled from that in case (a), one can see that the pressure inside the microcrack becomes more uniform. This would lead to the altered tissue deformation of the microcrack. Figure 10 illustrates the tapered microcrack when the permeability is the smallest among the three cases. When the permeability increases in case (b) and case (c), the almost uniform pressure field along the microcrack causes the more uniform deformation in the lateral direction of the microcrack. As a result, the volume of the enlarged microcrack increases. Note that, in the baseline simulation (case (a)), the enlarged microcrack's volume is 2.26 times the value of the original cylindrical microcrack. Decreasing or increasing the permeability by 50% from the baseline case would result in a microcrack volume of 1.9 times or 2.6 times the value of the original cylindrical microcrack.

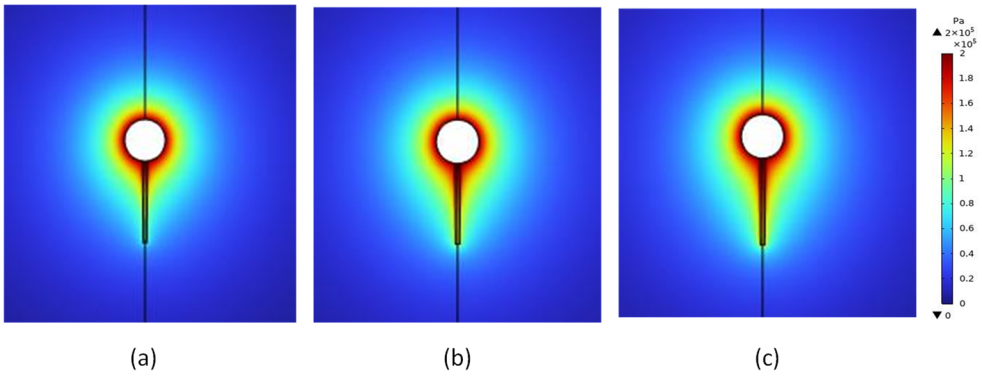

Figure 9. Details of the pressure field near the infusion surface and along the microcrack as influenced by the permeability of the microcrack: (**a**) $K_2 = 1 \times 10^{-13}$ m^2, (**b**) $K_2 = 2.0173 \times 10^{-13}$ m^2, and (**c**) $K_2 = 3 \times 10^{-13}$ m^2.

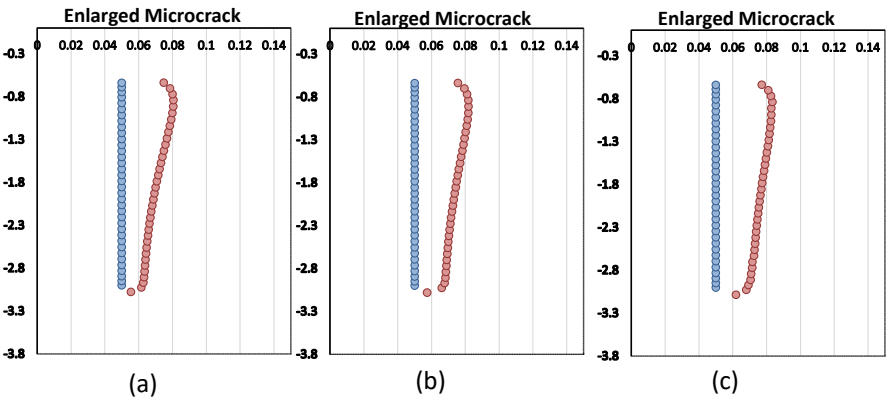

Figure 10. The original (blue dots) and post-deformation (orange dots) interfaces between the microcrack and tumor region, as affected by the permeability of the microcrack: (**a**) $K_2 = 1 \times 10^{-13}$ m^2, (**b**) $K_2 = 2.0173 \times 10^{-13}$ m^2, and (**c**) $K_2 = 3 \times 10^{-13}$ m^2.

The flow resistance as affected by the permeability of the microcrack is listed in Table 8. In the second model without tissue deformation, doubling or tripling the permeability in the microcrack would increase the reduction in the flow resistance from that without a microcrack by 3.2% or 5.0%, respectively. When the microcrack is enlarged in the third model, the reductions are 4.3% and 7.2% greater, respectively. Overall, the smallest flow resistance is found when the permeability is 3×10^{-13} m^2 with an enlarged microcrack. When compared to the flow resistance in the tumor without a microcrack, this reduction could be as large as 17% (1.94×10^{14} Pa s/m^3 vs. 2.33×10^{14} Pa s/m^3).

Table 8. Flow resistance due to differences in the permeability of the microcrack.

Permeability (m^2)	Flow Resistance (Pa s/m^3)			Reduction in Flow Resistance		
	1st Model	2nd Model	3rd Model	1st Model	2nd Model	3rd Model
1×10^{-13}	2.33×10^{14}	2.19×10^{14}	2.09×10^{14}	N/A	N/A	N/A
2.0173×10^{-13}	2.33×10^{14}	2.12×10^{14}	2.00×10^{14}	0%	3.2%	4.3%
3×10^{-13}	2.33×10^{14}	2.08×10^{14}	1.94×10^{14}	0%	5.0%	7.2%

3.3.4. Changing the Interstitial Fluid Pressure at the Infusion Surface

During an infusion process, the pressure at the infusion surface would significantly affect the total volumetric flow rate; however, it should not influence the total flow resistance if no deformation is considered. With tissue deformation as a factor, a larger infusion pressure would result in a larger enlargement in the microcrack, thus leading to smaller flow resistance. This section seeks to quantify the influence of the pressure at the infusion surface by varying it from 1×10^5 Pa to 2×10^5 Pa and subsequently to 4×10^5 Pa.

Figure 11 provides the displacement of the microcrack–tumor interface during the infusion process. As expected, the lateral displacement component of the interface is approximately proportional to the infusion pressure. The maximal lateral displacement increases 2.17-fold when the infusion pressure is doubled from 1×10^5 Pa to 2×10^5 Pa. Doubling the infusion pressure again to 4×10^5 Pa results in a 4.22-times increase from the first model.

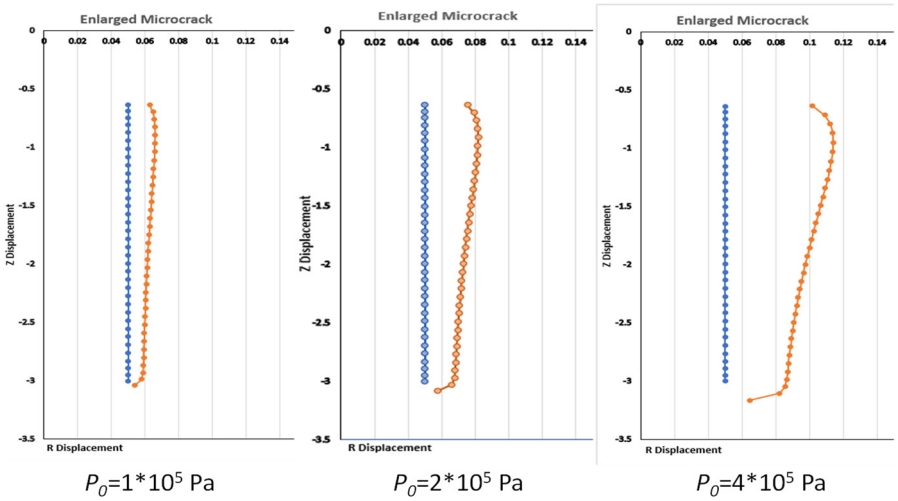

Figure 11. Obtained enlargements of the microcrack from the original locations (blue dots) to later locations (orange dots) at different infusion pressures.

The values of the flow resistance as affected by different infusion pressures are shown in Table 9. The results demonstrate that the flow resistance is independent of the infusion pressure in a tumor without tissue deformation, in the first and second models. The flow resistance decreases by 2.5% or 6.8% when the infusion pressure is doubled or quadrupled,

respectively, in the third model with tissue deformation. This observation suggests that, at higher pressure, the deformation of the tissue matrix enables easier fluid movement, thereby resulting in smaller flow resistance. Compared to the first model without a microcrack, the flow resistance with an enlarged microcrack is 18% smaller when the infusion pressure is 4×10^5 Pa.

Table 9. Flow resistance due to different infusion pressures.

Pressure (Pa)	Flow Resistance (Pa s/m^3)			Reduction in Flow Resistance		
	1st Model	2nd Model	3rd Model	1st Model	2nd Model	3rd Model
1×10^5	2.33×10^{14}	2.12×10^{14}	2.05×10^{14}	N/A	N/A	N/A
2×10^5	2.33×10^{14}	2.12×10^{14}	2.00×10^{14}	0%	0%	2.5%
4×10^5	2.33×10^{14}	2.12×10^{14}	1.91×10^{14}	0%	0%	6.8%

4. Discussion

This study contributes to the field of tumor treatment by providing a quantitative assessment of a novel method for the convection-enhanced delivery of drug-carrying nanofluids. This method is innovative as it introduces a microcrack and expands the microcrack due to tissue deformation. The results suggest that this is a viable option for the minimization of backflow and the delivery of drugs to the entire tumor. Up to 18% of the flow resistance reduction is predicted by an enlarged microcrack using the parameters in this study. It is anticipated that introducing multiple microcracks, as shown using retractable tines, would provide a significant resistance reduction. Therefore, it will decrease the pressure in the vicinity of the infusion catheter to minimize the deformation there and attenuate the backflow of the nanofluid. With minimal backflow through the catheter track, more drug-carrying nanostructures would be delivered to cover the entire tumor.

One limitation of this study is the inability to properly integrate Darcy's pressure field with the tissue deformation in the numerical models. A two-way coupling system that allows the pressure field and tissue deformation to impact each other would be ideal in gaining thorough knowledge of the fluid dynamics and tissue response in the tumor environment. However, due to the limitations of the computational tools utilized in this investigation, the module used could only deal with small material deformation, leading to one-way coupling only. This means that, while the pressure field can affect tissue deformation, the updated tissue geometry cannot change the pressure field. To address this shortcoming, a third model is created, which includes an enlarged microcrack based on the geometry produced from the second model's poroelastic simulation of tissue deformation. The current work provides a workaround; it does not fully depict the dynamic interaction of the fluid pressure and tissue deformation that happens in vivo. For example, tissue deformation would change the porosity of the tumor, which could influence the pressure and velocity fields in Darcy's law. We contacted COMSOL's technical support, and, after several rounds of discussion, we were informed that extra COMSOL modules would need to be added to our license. We are aware that, with the updated modules, two-way coupling modeling using COMSOL is possible, as shown by other research groups [37]. This is a limitation of our study, since we were not able to explore the coupling feature due to the lack of research resources at our institution. Other options to implement two-way coupling may include utilizing other commercial software packages. For example, FEBio, ABACUS, and ANSYS are some of the finite element method simulation packages to explore. The shortcoming of the current study highlight the need for more advanced computational tools or software advancements that can handle fully coupled simulations, allowing for the more realistic simulation of the intricate interactions occurring within the tumor microenvironment during convection-enhanced drug delivery.

In this study, our focus is on the overall resistance reduction induced by the microcrack, without including a backflow channel in the vicinity of an infusion catheter. Without a microcrack, backflow along an infusion catheter occurs, and it is significant. There is strong evidence that adding a microcrack would cause some fluid to flow through the enlarged microcrack, therefore alleviating the backflow along the infusion catheter. However, the extent of this is unknown. Therefore, incorporating an infusion catheter with tissue deformation into the current model would allow the thorough evaluation of whether the inclusion of microcracks effectively reduces backflow and improves therapeutic agent targeting. One could also explore the minimal number of microcracks necessary to significantly decrease backflow. One previous study implemented an infusion catheter with three retractable tines (Rex Medical) in patients [24]. They found that, using the retractable tines to infuse ethanol to liver tumors, most patients did not experience the reflex pain typically experienced when ethanol leaks through the backflow channel. This indicates that the three microcracks facilitated the flow in the tumors, resulting in smaller backflow along the infusion catheter. In addition, theoretical simulations could be developed to achieve the more realistic representation of CED devices and their effects on the backflow. This will entail not only fine-tuning the computational models but also undertaking experimental validation to guarantee that the theoretical insights are transferable to real applications in medication delivery.

Another noteworthy constraint of this study is its dependence on theoretical models with uniform transport and mechanical properties, as opposed to integrating empirical data on authentic tumor specimens. While the simulations quantify the possible influences of microcrack introduction on medication delivery in tumors, the lack of experimental validation with actual tumor tissue restricts the capacity to corroborate the findings' relevance in a real-world setting. The simplified model may fail to reflect the intricacies and heterogeneities of real tumors, reducing the efficacy of convection-enhanced delivery (CED) in clinical situations. In future studies, one could model the transport process based on reconstructed realistic tumor models from imaging scans. Different layers/regions with various transport properties could be included in the model. The modeling of the pressure and velocity fields in realistic tumors with complexity and heterogeneity would enhance the prediction capabilities of theoretical simulations.

One future study could be focused on nanostructure transport in tumors. In the current model, we only simulate the fluid pressure field and velocity field. The current simulation can be extended to simulate drug-carrying nanoparticle diffusion and convection in the tumor. With the simulated fluid field, the transient process of nanoparticle spreading in the tumor can be evaluated to understand the infusion duration and other strategies for nanoparticle deposition in tumors.

Finally, although the use of microcracks has shown promise in improving therapeutic drug delivery to tumors, the dynamic interaction between the microcrack and its surrounding tissue is unknown. The introduction of microcracks may impair the structural and functional integrity of the tumor's extracellular matrix, resulting in unexpected consequences such as inflammation, edema, or even neuronal injury. Furthermore, the long-term stability of these microcracks, as well as their propensity to mend or spread further, requires future investigation, seeking to employ an effective yet safe delivery method for the treatment of tumors. Moreover, experimental studies are warranted to evaluate the performance of the proposed approach in tissue-equivalent gels, as well as in biological tissue. Transparent gels would be very useful to observe progressing crack enlargement and fluid flow pathways. In vivo or in vitro experiments on animal tissue are also critical to understand the interaction between the microcrack and the surrounding tissue. Experimental validation is necessary to not only provide the extracted transport properties needed for theoretical simulations, but also to help evaluate the assumptions and simplifications made in the theoretical models. By comparing the simulation results to experimental results, researchers may detect differences and improve the theoretical models to better reflect the behavior of therapeutic drugs in actual tumors. A future comparison study would give

useful inputs on the accuracy and relevance of simulation-based predictions, resulting in accurate and successful tumor treatment.

5. Conclusions

This study presents the quantification of the improvement in drug delivery to tumors in convection-enhanced delivery (CED) via the manipulation of a microcrack within a tumor. We perform theoretical simulations to evaluate how the introduction of a microcrack in tissue reduces the overall flow resistance in a porous tumor, as well as further decreasing as the microcrack enlarges in a direct infusion process using CED. It is found that the presence of a microcrack leads to significant modifications in the tumor pressure and tissue displacement fields, with the fluid pressure field causing the cylindrical microcrack to expand into a frustum shape. This enlargement results in the more than doubling of the microcrack volume, indicating a substantial increase in the available space for fluid flow. The introduction of an enlarged microcrack leads to a reduction in flow resistance of 14% compared to the tumor without a microcrack. In the parametric analyses, a larger microcrack radius, a longer microcrack, and/or a larger infusion pressure result in more significant decreases in the flow resistance in the tumor, up to 18% from the tumor without a microcrack. In conclusion, the findings from this study suggest that introducing a microcrack into porous tumors is an effective strategy to enhance the fluid flow and, consequently, the distribution of therapeutic agents using CED. By reducing the flow resistance and facilitating the more uniform dispersion of drugs, microcrack formation and enlargement emerge as promising techniques to improve the efficacy of cancer treatment in porous tumor environments.

Author Contributions: Conceptualization, L.Z. and R.M.; methodology, M.J.N., R.M. and L.Z.; software, M.J.N. and R.M.; formal analysis, M.J.N. and L.Z.; writing—original draft preparation, M.J.N. and L.Z.; writing—review and editing, R.M. and L.Z. All authors have read and agreed to the published version of the manuscript.

Funding: This research received no external funding.

Data Availability Statement: The original contributions presented in the study are included in the article, further inquiries can be directed to the corresponding author.

Conflicts of Interest: The authors declare no conflicts of interest.

References

1. Wilhelm, S.; Tavares, A.J.; Dai, Q.; Ohta, S.; Audet, J.; Dvorak, H.F.; Chan, W.C.W. Analysis of nanoparticle delivery to tumours. *Nat. Rev. Mater.* **2016**, *1*, 16014. [CrossRef]
2. Begg, K.; Tavassoli, M. Inside the hypoxic tumour: Reprogramming of the DDR and radioresistance. *Cell Death Discov.* **2020**, *6*, 77. [CrossRef] [PubMed]
3. Bauer, H.-C.; Krizbai, I.A.; Bauer, H.; Traweger, A. You shall not pass"—Tight junctions of the blood brain barrier. *Front. Neurosci.* **2014**, *8*, 392. [CrossRef] [PubMed]
4. McGuire, S.; Zaharoff, D.; Yuan, F. Nonlinear dependence of hydraulic conductivity on tissue deformation during intratumoral infusion. *Ann. Biomed. Eng.* **2006**, *34*, 1173–1181. [CrossRef] [PubMed]
5. Jahangiri, A.; Chin, A.T.; Flanigan, P.M.; Chen, R.; Bankiewicz, K.; Aghi, M.K. Convection-enhanced delivery in glioblastoma: A review of preclinical and clinical studies. *J. Neurosurg.* **2017**, *126*, 191–200. [CrossRef]
6. Zhou, Z.; Singh, R.; Souweidane, M.M. Convection-enhanced delivery for diffuse intrinsic pontine glioma treatment. *Curr. Neuropharmacol.* **2017**, *15*, 116–128. [CrossRef]
7. Mehta, A.I.; Choi, B.D.; Raghavan, R.; Brady, M.; Friedman, A.H.; Bigner, D.D.; Pastan, I.; Sampson, J.H. Imaging of convection enhanced delivery of toxins in humans. *Toxins* **2011**, *3*, 201–206. [CrossRef]
8. Lonser, R.R.; Sarntinoranont, M.; Morrison, P.F.; Oldfield, E.H. Convection-enhanced delivery to the central nervous system. *J. Neurosurg.* **2015**, *122*, 697–706. [CrossRef]
9. Raghavan, R.; Brady, M.L.; Rodríguez-Ponce, M.I.; Hartlep, A.; Pedain, C.; Sampson, J.H. Convection-enhanced delivery of therapeutics for brain disease, and its optimization. *Neurosurg. Focus* **2006**, *20*, E12. [CrossRef]
10. Casanova, F.; Carney, P.R.; Sarntinoranont, M. Effect of needle insertion speed on tissue injury, stress, and backflow distribution for convection-enhanced delivery in the rat brain. *PLoS ONE* **2014**, *9*, e94919. [CrossRef]

11. Hines-Peralta, A.; Liu, Z.-J.; Horkan, C.; Solazzo, S.; Goldberg, S.N. Chemical tumor ablation with use of a novel multiple-tine infusion system in a canine sarcoma model. *J. Vasc. Interv. Radiol.* **2006**, *17*, 351–358. [CrossRef] [PubMed]
12. Orozco, G.A.; Smith, J.H.; García, J.J. Three-dimensional nonlinear finite element model to estimate backflow during flow-controlled infusions into the brain. *Proc. Inst. Mech. Eng. Part H J. Eng. Med.* **2020**, *234*, 1018–1028. [CrossRef] [PubMed]
13. Orozco, G.; Córdoba, G.; Urrea, F.; Casanova, F.; Smith, J.; García, J. Finite element model to reproduce the effect of pre-stress and needle insertion velocity during infusions into brain phantom gel. *IRBM* **2021**, *42*, 180–188. [CrossRef]
14. Ayers, A.D.; Smith, J.H. A biphasic fluid–structure interaction model of backflow during infusion into agarose gel. *J. Biomech. Eng.* **2023**, *145*, 121009. [CrossRef]
15. Su, D.; Ma, R.; Zhu, L. Numerical study of nanofluid infusion in deformable tissues in hyperthermia cancer treatment. *Med. Biol. Eng. Comput.* **2011**, *11*, 1233–1240. [CrossRef]
16. Sillay, K.A.; McClatchy, S.G.; Shepherd, B.A.; Venable, G.T.; Fuehrer, T.S. Image-guided convection-enhanced delivery into agarose gel models of the brain. *J. Vis. Exp.* **2014**, *14*, 51466. [CrossRef]
17. Lonser, R.R.; Walbridge, S.; Garmestani, K.; Butman, J.A.; Walters, H.A.; Vortmeyer, A.O.; Morrison, P.F.; Brechbiel, M.W.; Oldfield, E.H. Successful and safe perfusion of the primate brainstem: In vivo magnetic resonance imaging of macromolecular distribution during infusion. *J. Neurosurg.* **2002**, *97*, 905–913. [CrossRef]
18. Krauze, M.T.; Saito, R.; Noble, C.; Tamas, M.; Bringas, J.; Park, J.W.; Berger, M.S.; Bankiewicz, K. Reflux-free cannula for convection-enhanced high-speed delivery of therapeutic agents. *J. Neurosurg.* **2005**, *103*, 923–929. [CrossRef]
19. Morrison, P.F.; Chen, M.Y.; Chadwick, R.S.; Lonser, R.R.; Oldfield, E.H. Focal delivery during direct infusion to brain: Role of flow rate, catheter diameter, and tissue mechanics. *Am. J. Physiol.-Regul. Integr. Comp. Physiol.* **1999**, *277*, R1218–R1229. [CrossRef]
20. Chen, M.Y.; Lonser, R.R.; Morrison, P.F.; Governale, L.S.; Oldfield, E.H. Variables affecting convection-enhanced delivery to the striatum: A systematic examination of rate of infusion, cannula size, infusate concentration, and tissue—Cannula sealing time. *J. Neurosurg.* **1999**, *90*, 315–320. [CrossRef]
21. Debinski, W.; Tatter, S. Convection-enhanced delivery for the treatment of brain tumors. *Expert Rev. Neurother.* **2009**, *9*, 1519–1527. [CrossRef] [PubMed]
22. Bidros, D.S.; Liu, J.K.; Vogelbaum, M.A. Future of convection-enhanced delivery in the treatment of brain tumors. *Future Oncol.* **2010**, *6*, 117–125. [CrossRef] [PubMed]
23. Seunguk, O.; Odland, R.; Wilson, S.R.; Kroeger, K.M.; Liu, C.; Lowenstein, P.R.; Castro, M.G.; Hall, W.A.; Ohlfest, J.R. Improved distribution of small molecules and viral vectors in the murine brain using a hollow fiber catheter. *J. Neurosurg.* **2007**, *107*, 568–577.
24. Kuang, M.; Lu, M.-D.; Xie, X.-Y.; Xu, H.-X.; Xu, Z.-F.; Liu, G.-J.; Yin, X.-Y.; Huang, J.-F.; Lencioni, R. Ethanol ablation of hepatocellular carcinoma Up to 5.0 cm by using a multipronged injection needle with high-dose strategy. *Radiology* **2009**, *253*, 552–561. [CrossRef]
25. Khaled, A.-R.; Vafai, K. The role of porous media in modeling flow and heat transfer in biological tissues. *Int. J. Heat Mass Transf.* **2003**, *46*, 4989–5003. [CrossRef]
26. Truskey, G.A.; Yuan, F.; Katz, D.F. *Transport Phenomena in Biological Systems*, 2nd ed.; Pearson Prentice Hall: Upper Saddle River, NJ, USA, 2009.
27. Chen, Z.-J.; Broaddus, W.C.; Viswanathan, R.R.; Raghavan, R.; Gillies, G.T. Intraparenchymal drug delivery via positive-pressure infusion: Experimental and modeling studies of poroelasticity in brain phantom gels. *IEEE Trans. Biomed. Eng.* **2002**, *49*, 85–96. [CrossRef]
28. Chen, X.; Sarntinoranont, M. Biphasic finite element model of solute transport for direct infusion into nervous tissue. *Ann. Biomed. Eng.* **2007**, *35*, 2145–2158. [CrossRef]
29. Lai, W.M.; Mow, V.C. Drag-induced compression of articular cartilage during a permeation experiment. *Biorheology* **1980**, *17*, 111–123. [CrossRef]
30. Sobey, I.; Wirth, B. Effect of non-linear permeability in a spherically symmetric model of hydrocephalus. *Math. Med. Biol.* **2006**, *23*, 339–361. [CrossRef]
31. Stylianopoulos, T.; Martin, J.D.; Chauhan, V.P.; Jain, S.R.; Diop-Frimpong, B.; Bardeesy, N.; Smith, B.L.; Ferrone, C.R.; Hornicek, F.J.; Boucher, Y. Causes, consequences, and remedies for growth-induced solid stress in murine and human tumors. *Proc. Natl. Acad. Sci. USA* **2012**, *109*, 15101–15108. [CrossRef]
32. Skalak, R.; Zargaryan, S.; Jain, R.K.; Netti, P.A.; Hoger, A. Compatibility and the genesis of residual stress by volumetric growth. *J. Math. Biol.* **1996**, *34*, 889–914. [CrossRef] [PubMed]
33. Basser, P.J. Interstitial pressure, volume, and flow during infusion into brain tissue. *Microvasc. Res.* **1992**, *44*, 143–165. [CrossRef] [PubMed]
34. Netti, P.A.; Baxter, L.T.; Boucher, Y.; Skalak, R.; Jain, R.K. Macro-and microscopic fluid transport in living tissues: Application to solid tumors. *AIChE J.* **1997**, *43*, 818–834. [CrossRef]
35. Singh, M.; Ma, R.; Zhu, L. Theoretical evaluation of enhanced gold nanoparticle delivery to pc3 tumors due to increased hydraulic conductivity or recovered lymphatic function after mild whole body hyperthermia. *Med. Biol. Eng. Comput.* **2021**, *59*, 301–313. [CrossRef]

36. Naseem, M.J.; Ma, R.; Zhu, L. Enhancing fluid infusion via introduction and enlargement of microcrack in tumors—Theoretical simulations. In Proceedings of the Summer Biomechanics, Bioengineering and Biotransport Conference, Lake Geneva, WI, USA, 11–14 June 2024; Submission ID: 243.
37. Yuan, T.; Shen, L.; Dini, D. Porosity-permeability tensor relationship of closely and randomly packed fibrous biomaterials and biological tissues: Application to the brain white matter. *Acta Biomater.* **2024**, *173*, 123–134. [CrossRef] [PubMed]